

Critical Evaluations and Thermodynamic Optimizations of the MnO-Mn₂O₃-SiO₂ and FeO-Fe₂O₃-MnO-Mn₂O₃-SiO₂ Systems



YOUN-BAE KANG and IN-HO JUNG

A critical evaluation and thermodynamic modeling for thermodynamic properties of all oxide phases and phase diagrams in the Fe-Mn-Si-O system (MnO-Mn₂O₃-SiO₂ and FeO-Fe₂O₃-MnO-Mn₂O₃-SiO₂ systems) are presented. Optimized Gibbs energy parameters for the thermodynamic models of the oxide phases were obtained which reproduce all available and reliable experimental data within error limits from 298 K (25 °C) to above the liquidus temperatures at all compositions covering from known oxide phases, and oxygen partial pressure from metal saturation to 0.21 bar. The optimized thermodynamic properties and phase diagrams are believed to be the best estimates presently available. Slag (molten oxide) was modeled using the modified quasichemical model in the pair approximation. Olivine (Fe₂SiO₄-Mn₂SiO₄) was modeled using two-sublattice model in the framework of the compound energy formalism (CEF), while rhodonite (MnSiO₃-FeSiO₃) and braunite (Mn₇SiO₁₂ with excess Mn₂O₃) were modeled as simple Henrian solutions. It is shown that the already developed models and databases of two spinel phases (cubic- and tetragonal-(Fe, Mn)₃O₄) using CEF [Kang and Jung, *J. Phys. Chem. Solids* (2016), vol. 98, pp. 237–246] can successfully be integrated into a larger thermodynamic database to be used in practically important higher order system such as silicate. The database of the model parameters can be used along with a software for Gibbs energy minimization in order to calculate any type of phase diagram section and thermodynamic properties.

DOI: 10.1007/s11663-017-0953-5

© The Minerals, Metals & Materials Society and ASM International 2017

I. INTRODUCTION

THE iron-manganese silicate has been of particular interest in steel industries. Reduction of ores in blast furnace results in forming silicate slags in which iron and manganese oxides dissolve. Deoxidation of liquid steel with FeSi alloy or MnSi alloy results in oxide inclusions in steel.^[1,2] Understanding surface/internal oxidation of steel slab during reheating process requires thermodynamics of the iron-manganese silicate.^[3,4] Therefore, knowledge of thermodynamics and phase equilibria on Fe-Mn-Si oxide systems should give valuable information in practical operation. In theoretical view, this system is also interesting to model, because Fe and Mn are both transition metals: stability of Fe-Mn oxides is sensitive to oxygen partial pressure exerted on the oxides. Therefore, it is required to understand thermodynamics and phase equilibria in this system, and thermodynamic modeling and database construction of this system should be very useful.

Such thermodynamic database can be prepared by critical evaluation, thermodynamic modeling, and optimization. In a thermodynamic “optimization,” adjustable Gibbs energy model parameters are optimized in order to reproduce all available and reliable thermodynamic and phase equilibrium data. This gives one set of model equations as functions of temperature, pressure, and composition. Thermodynamic data, such as activities, can aid in the evaluation of the phase diagrams, and information on phase equilibria can be used to deduce thermodynamic properties. Thus, it is frequently possible to resolve discrepancies in the available data. From the model equations, all of the thermodynamic properties and phase diagrams can be back-calculated, and interpolations and extrapolations can be made in a thermodynamically correct manner. The data are, thereby, rendered self-consistent and compliant with thermodynamic principles, and the available data are distilled into a small set of model parameters, which is ideal for computer storage.

Thermodynamic evaluations and optimizations for several sub-systems of the FeO-Fe₂O₃-MnO-Mn₂O₃-SiO₂ system were previously carried out for the Fe-O system,^[5] the Mn-O system,^[6] the Fe-Mn-O system,^[7–9] the FeO-Fe₂O₃-SiO₂ system,^[10] MnO-SiO₂ system,^[11] respectively. All these work employed the modified quasichemical model (MQM) in the pair approximation^[12–14] in order to model liquid oxide. These previous works were taken in the present study directly without

YOUN-BAE KANG is with the Graduate Institute of Ferrous Technology, Pohang University of Science and Technology, Pohang, 37673, Republic of Korea. Contact e-mail: ybkang@postech.ac.kr
IN-HO JUNG is with the Department of Mining and Materials Engineering, McGill University Montreal, Montreal, QC, H3A 2B2, Canada.

Manuscript submitted September 18, 2016.
Article published online March 13, 2017.

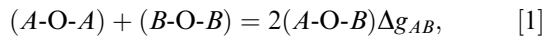
any modification. The present study is a part of a complete database development of the $\text{Al}_2\text{O}_3\text{-CaO-FeO-Fe}_2\text{O}_3\text{-MgO-MnO-Mn}_2\text{O}_3\text{-SiO}_2$ systems for applications in the ferrous, non-ferrous, ceramic, and electric/electronic industries. All the thermodynamic calculations in the present study were carried out using FactSage.^[15–17]

II. THERMODYNAMIC MODELS

Figures 1 to 5 show calculated phase diagrams of sub-systems of the present $\text{FeO-Fe}_2\text{O}_3\text{-MnO-Mn}_2\text{O}_3\text{-SiO}_2$ system; $\text{FeO-Fe}_2\text{O}_3\text{-SiO}_2$ system,^[10] MnO-SiO_2 system,^[7] Fe-O system,^[5] Mn-O system,^[6] and Fe-Mn-O system,^[8,9] previously thermodynamically modeled. A number of phases were identified including various solid solutions, solid compounds, and liquid oxide phase. Therefore, it is useful to see what kinds of phases appear in the system at a glance. Figure 6 shows a schematic representation of the $\text{FeO-MnO-SiO}_2\text{-O(-Fe-Mn-Si)}$ system (oxide) with stable phases. Moving towards O corner represents “oxidation,” on the other hand, moving away from the O corner represents “reduction.” All the stable phases observed in the system are listed in Table I.

A. Slag (Molten Oxide)

For the slag (molten oxide) phase, the MQM in the pair approximation was used.^[12,13] This model has been recently further developed and summarized.^[14,18] Short-range-ordering is taken into account by considering second-nearest-neighbor (SNN) pair exchange reactions. For example, for the $\text{FeO-MnO-FeO}_{1.5}\text{-MnO}_{1.5}\text{-SiO}_2$ slag, this reaction is:



where $(i\text{-O-}j)$ represents a SNN pair, and A and B stand for Fe^{2+} , Mn^{2+} , Fe^{3+} , Mn^{3+} , and Si^{4+} ,

respectively. Parameters of the model are a set of Gibbs energies of these reactions, Δg_{AB} , which may be expanded as empirical functions of composition and temperature.

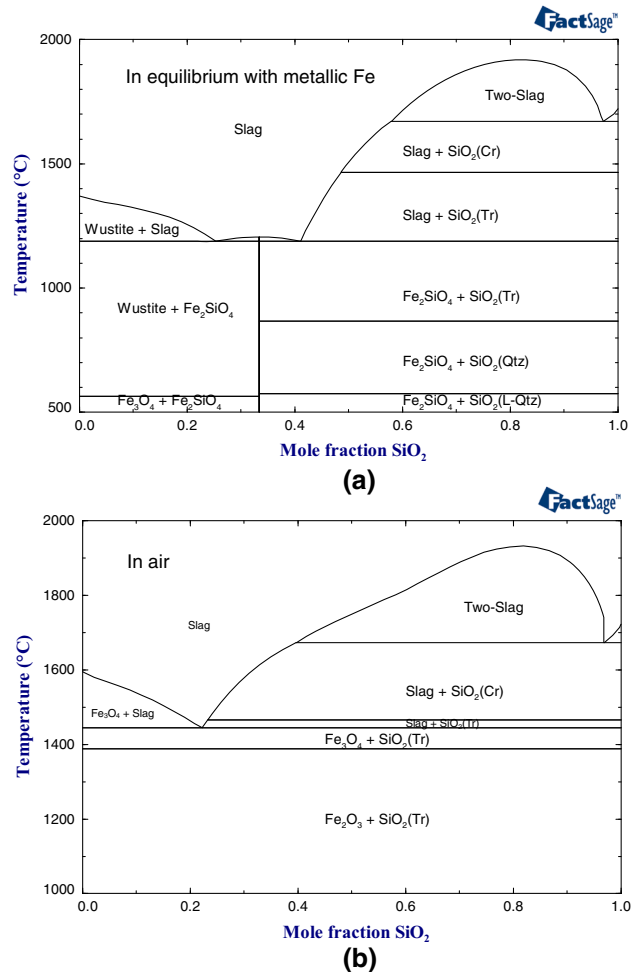


Fig. 1—Optimized phase diagram of the $\text{FeO-Fe}_2\text{O}_3\text{-SiO}_2$ system (a) in equilibrium with metallic Fe and (b) in air.^[10]

Table I. Stable Phases Observed in the $\text{FeO-Fe}_2\text{O}_3\text{-MnO-Mn}_2\text{O}_3\text{-SiO}_2$ System

Names	Composition [†]	Space Groups	Pearson Symbols	Prototypes
Manganowüstite (MW)	$(\text{Fe}^{2+}, \text{Mn}^{2+}, \text{Fe}^{3+}, \text{Mn}^{3+})_{1-\delta}\text{O}$	$Fm\bar{3}m$	$cF8$	NaCl
Tetragonal Spinel (T.Sp)	$(\text{Fe}^{2+}, \text{Fe}^{3+}, \text{Mn}^{2+}, \text{Mn}^{3+})_{3-\Delta}\text{O}_4$	$I4_1/amd$	$tI28$	$\alpha\text{-Mn}_3\text{O}_4$
Spinel (C.Sp)	$(\text{Fe}^{2+}, \text{Fe}^{3+}, \text{Mn}^{2+}, \text{Mn}^{3+}, \text{Mn}^{4+})_{3-\Delta}\text{O}_4$	$Fd\bar{3}m$	$cF56$	MgAl_2O_4
β -Bixbyite (Bix)	$(\text{Mn}^{3+}, \text{Fe}^{3+})_2\text{O}_3$	$Ia\bar{3}$	$cI80$	$\beta\text{-Mn}_2\text{O}_3$
α -Bixbyite	Mn_2O_3	—	—	—
Hematite (Hem)	$(\text{Fe}^{3+}, \text{Mn}^{3+})_2\text{O}_3$	$R\bar{3}c$	$hR10$	$\alpha\text{-Al}_2\text{O}_3$
Rhodonite (Rho)	$(\text{Mn}^{2+}, \text{Fe}^{2+})\text{SiO}_3$	$P\bar{1}$	—	MnSiO_3
Olivine (Oli)	$(\text{Mn}^{2+}, \text{Fe}^{2+})_2\text{SiO}_4$	$Pbnm$	$oP28$	Mg_2SiO_4
Braunite (Brn)	Mn_6^{3+} (“ $\text{Mn}^{2+}\text{Si}^{4+}$,” “ $\text{Mn}^{3+}\text{Mn}^{3+}$ ”) O_{12}	$I4_1/acd$	—	$\text{Mn}_7\text{SiO}_{12}$
Quartz (L-Qtz)	SiO_2	$P3_21$	$hP9$	$\alpha\text{-quartz}$
Quartz (Qtz)	SiO_2	$P6_222$	$hP9$	$\beta\text{-quartz}$
Tridymite (Tr)	SiO_2	$P6_3/mmc$	$hP12$	$\beta\text{-tridymite}$
Cristobalite (Cr)	SiO_2	$Fd\bar{3}m$	$cF24$	$\beta\text{-cristobalite}$
Slag	$(\text{Fe}^{2+}, \text{Fe}^{3+}, \text{Mn}^{2+}, \text{Mn}^{3+}, \text{Si}^{4+})_x\text{O}_y$	—	—	—

[†] Components in *italic* dissolve into the phase by limited amount. Model structures were given in the text (see Section II).

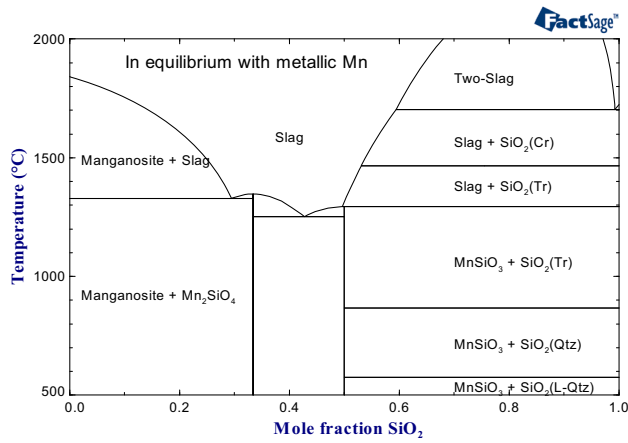


Fig. 2—Optimized phase diagram of the MnO-Mn₂O₃-SiO₂ system in equilibrium with metallic Mn.^[11]

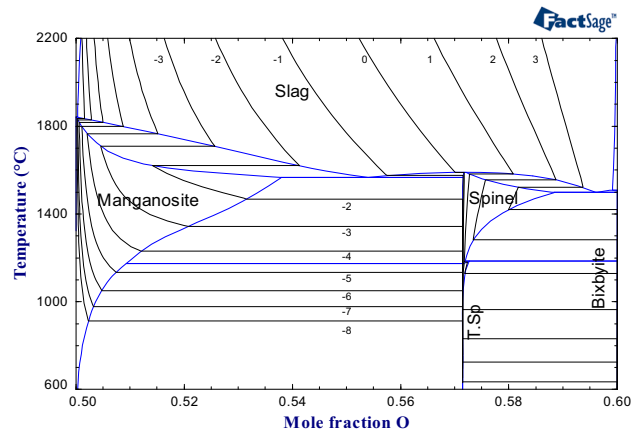


Fig. 4—Optimized phase diagram of the Mn-O system.^[6] Thin lines represent logarithm of oxygen partial pressure.

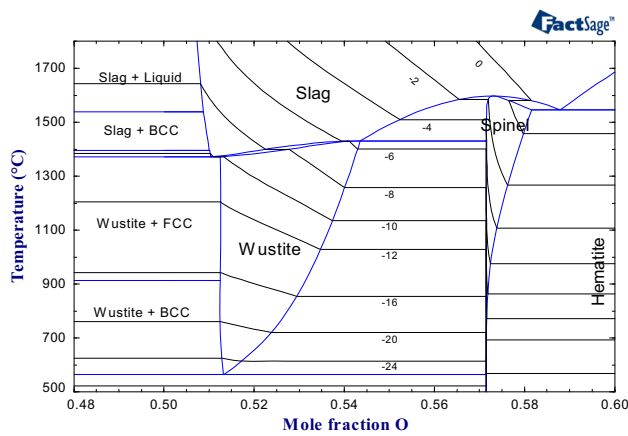


Fig. 3—Optimized phase diagram of the Fe-O system.^[5] Thin lines represent logarithm of oxygen partial pressure.

$$\Delta g_{AB} = \Delta g_{AB}^{\circ} + \sum_{ij} q_{AB}^{ij} Y_A^i Y_B^j, \quad [2]$$

where Y_i is the equivalent fraction of the component i , which is composed of number of moles of i and its “coordination number”.^[14] “Coordination numbers” of all components required in the MQM were set to be 1.3774 (Fe²⁺ and Mn²⁺), 2.0662 (Fe³⁺ and Mn³⁺), and 2.7548 (Si⁴⁺), respectively.

Gibbs energy of pure liquid components were taken from Wu *et al.* for MnO,^[7] Kang and Jung for Mn₂O₃,^[6] Degterov *et al.* for FeO and Fe₂O₃,^[5] Eriksson and Pelton for SiO₂, respectively. “Toop-like” interpolation method proposed by Pelton was used in order to estimate Gibbs energy of this quaternary slag.^[18,20] Divalent cations (Fe²⁺ and Mn²⁺) and trivalent cations (Fe³⁺ and Mn³⁺) were set to one group, while tetravalent cation (Si⁴⁺) was set to the other group. Therefore, the Gibbs energy of sub-ternary system, for example FeO-Fe₂O₃-SiO₂, was estimated using the “Toop-like” interpolation method where SiO₂ was set as an

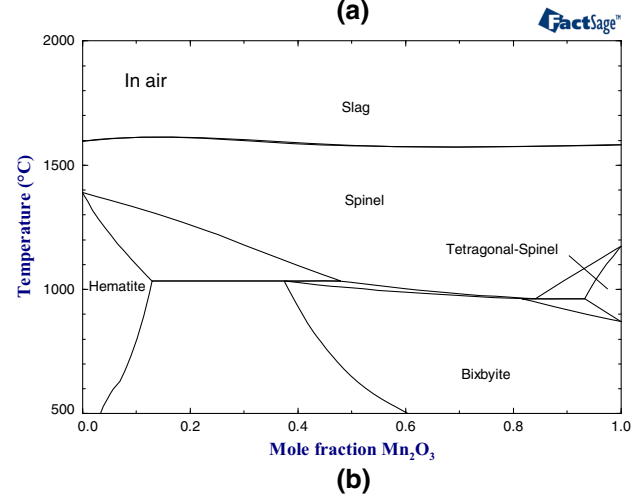
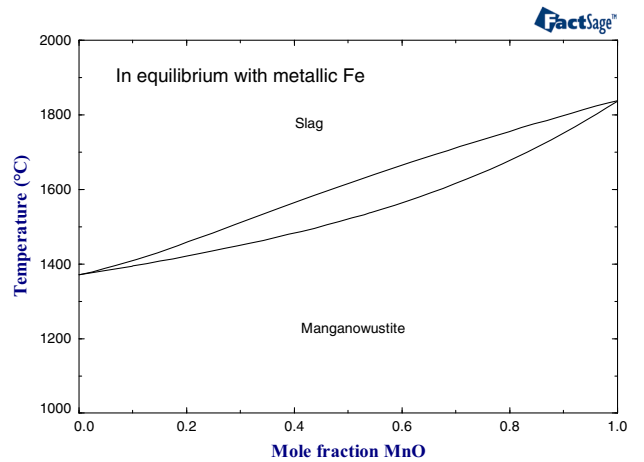


Fig. 5—Optimized phase diagram of the Fe-Mn-O system (a) in equilibrium with metallic Fe^[7] and (b) in air.^[8,9]

asymmetric component. In case of FeO-MnO-Fe₂O₃ sub-ternary system, “Kohler-like” interpolation method was used. The only exception was applied to MnO-Mn₂O₃-SiO₂ system where “Kohler-like” interpolation method was used, which was found to give the

best result. When it is necessary, small sizes of ternary parameters were added to some of Δg_{ABS} . Mathematical form of the ternary parameters are dependent on what kind of interpolation method was employed. Detailed formulation can be found in Reference 20, therefore, it is not repeated in the present article. The optimized thermodynamic values for the slag are shown in Table II.

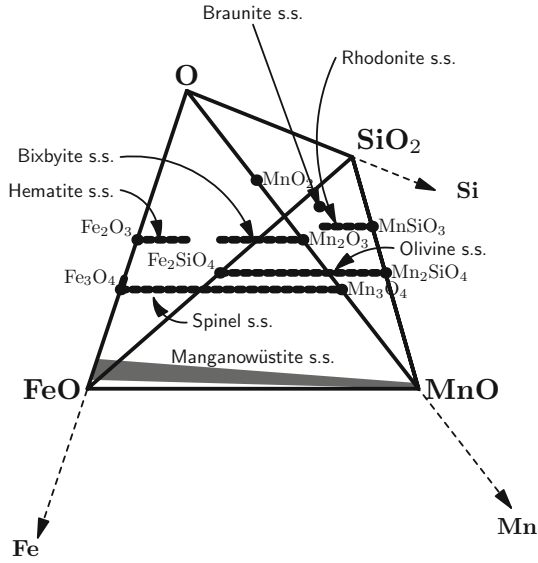
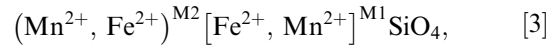


Fig. 6—Schematic representation of phases in the FeO-MnO-SiO₂-O(-Fe-Mn-Si) system showing all phases (except for slag) concerned in the present study.

B. Olivine

The olivine solid solution has an orthorhombic structure (*Pbnm*). Half of the octahedral sites are occupied by metallic atoms Mn and Fe, while one-eighth of tetrahedral sites are occupied by Si atoms. Besides, the octahedral sites are split into two sublattices, called M2 and M1^[21]:



where cations shown within a set of brackets occupy the same sublattice. Because M2 sites are larger than M1 sites, Mn²⁺ (which is larger than Fe²⁺)^[22] preferentially enters into the M2 sites. For the olivine solution, the model is developed within the framework of the compound energy formalism (CEF).^[23] The Gibbs energy expression in the CEF per formula unit of a solution is as follows:

$$G = \sum_i \sum_j y_i^{\text{M2}} y_j^{\text{M1}} G_{ij} - T\Delta S^{\text{config}} + G^E, \quad [4]$$

where y_i^{M2} and y_j^{M1} represent the site fractions of constituents i and j on the M2 and M1 sublattices, G_{ij} is the Gibbs energy of an “end-member” $(i)^{\text{M2}}(j)^{\text{M1}}\text{SiO}_4$, in which the M2 and M1 sublattices are occupied only by i and j cations, respectively. ΔS^{config} is the configurational entropy assuming random mixing on each sublattice given by:

$$\Delta S^{\text{config}} = -R \left(\sum_i y_i^{\text{M2}} \ln y_i^{\text{M2}} + \sum_j y_j^{\text{M1}} \ln y_j^{\text{M1}} \right), \quad [5]$$

Table II. Optimized Model Parameters for Slag, Olivine, Rhodonite, and Braunitz Phases (J/mol)

Slag: $(\text{FeO}-\text{MnO}-\text{FeO}_{1.5}-\text{MnO}_{1.5}-\text{SiO}_2)^{\ddagger, \S}$	
$q_{\text{MnO}_{1.5}, \text{SiO}_2}^{05}$	= 41,840
$q_{\text{MnO}, \text{SiO}_2, \text{MnO}_{1.5}}^{301}$	= -25,104
$q_{\text{FeO}, \text{MnO}, \text{SiO}_2}^{101}$	= -8368
$q_{\text{SiO}_2, \text{MnO}_{1.5}, \text{FeO}_{1.5}}^{002}$	= 25,104
Olivine: $(\text{Fe}^{2+}, \text{Mn}^{2+})^{\text{M2}}[\text{Fe}^{2+}, \text{Mn}^{2+}]^{\text{M1}}\text{SiO}_4^{\S}$	
G_{FF}	= $G_{\text{Fe}_2\text{SiO}_4}^{\circ}$ (fayalite)
G_{MM}	= $G_{\text{Mn}_2\text{SiO}_4}^{\circ}$ (tephroite)
I_{FM}	= $G_{\text{FF}} + G_{\text{MM}} - 2G_{\text{FM}} = -10,669$
$\Delta_{\text{FM:FM}}$	= $G_{\text{FF}} + G_{\text{MM}} - G_{\text{FM}} - G_{\text{MF}} = 0$
Rhodonite: $(\text{Mn}^{2+}, \text{Fe}^{2+})\text{SiO}_3^{\S, \#}$	
G_{FeSiO_3} (rhodonite)	= $G_{\text{FeSiO}_3}^{\circ}$ (orthopyroxene) - 469
Braunitz: $\text{Mn}_6^{3+}([\text{Mn}^{2+}\text{Si}^{4+}], [\text{Mn}^{3+}\text{Mn}^{3+}])\text{O}_{12}$	
$G_{[\text{MnSi}]}$	= $G_{\text{Mn}_7\text{SiO}_{12}}^{\circ}$ (braunitz)
$G_{[\text{MnMn}]}$	= -4,140,826.41 + 3763.47T - 591.51T ln T - 65,040.38 ln T
	= $4 \times G_{\text{Mn}_2\text{O}_3(\beta\text{-bixbyite})}^{\circ} + 8368$

[†] Gibbs energy of pure liquid components were taken from Wu *et al.* for MnO,^[7] Kang and Jung for Mn₂O₃^[6] Degterov *et al.* for FeO and Fe₂O₃,^[5] Eriksson and Pelton for SiO₂ respectively.

[‡] Parameters of the MQM used to model the slag are defined in Ref. [14,18].

[§] The Gibbs energies of Fe₂SiO₄(fayalite), Mn₂SiO₄(tephroite) and MnSiO₃(rhodonite) were taken from Jak *et al.*^[10] and Eriksson *et al.*^[11]

[#] Gibbs energies of FeSiO₃(orthopyroxene) was taken from Jung *et al.*^[15,25]

and G^E is the excess Gibbs energy given by:

$$G^E = \sum_i \sum_j \sum_k y_i^{M2} y_j^{M2} y_k^{M1} L_{ij:k} + \sum_i \sum_j \sum_k y_k^{M2} y_i^{M1} y_j^{M1} L_{k:ij}, \quad [6]$$

where $L_{ij:k}$ and $L_{k:ij}$ are interaction energies between cations i and j on one sublattice when the other sublattice is occupied only by cation k . For the olivine solution, there are four end-member Gibbs energies G_{FF} , G_{MM} , G_{FM} , and G_{MF} (where F and M denote Fe^{2+} and Mn^{2+} , respectively). G_{FF} is equal to $G^\circ(Fe_2SiO_4)$ which is the Gibbs energy of stoichiometric fayalite Fe_2SiO_4 . G_{MM} is equal to $G^\circ(Mn_2SiO_4)$ which is the Gibbs energy of stoichiometric tephroite (Mn_2SiO_4). Both of these Gibbs energies were optimized previously.^[10,11] The Gibbs energies G_{FM} and G_{MF} are model parameters which were optimized in the present study. However, rather than considering all these parameters independently, it is more physically meaningful to consider the linear combinations:

$$I_{FM} = G_{FF} + G_{MM} - 2G_{FM}, \quad [7]$$

$$\Delta_{FM:FM} = G_{FF} + G_{MM} - G_{FM} - G_{MF}. \quad [8]$$

I_{FM} has the physical significance of being equal to the energy change of the site exchange reaction when Fe^{2+} and Mn^{2+} , occupying M2 and M1 sites, respectively, change places. The linear combination $\Delta_{FM:FM}$ similarly has physical significance as the energy change of the “reciprocal exchange reaction” among end-members, which is typically close to zero. Setting $\Delta_{FM:FM}$ equal to zero is equivalent to assuming that the sum of the energies of a SNN Fe(M1)-Mn(M2) pair bond and a Mn(M1)-Fe(M2) pair bond is equal to the sum of the energies of a Fe(M1)-Fe(M2) and a Mn(M1)-Mn(M2) pair bond. Such a symmetrical assumption seems reasonable. For other olivine solutions, this term has been found empirically to be close to zero.^[24] Thus, in this study, $\Delta_{FM:FM}$ was set to be zero and only I_{FM} has been optimized. Optimized model parameters are listed in Table II.

C. Rhodonite

Relatively limited amount of iron can substitute for manganese in rhodonite, $MnSiO_3$ (triclinic, $P\bar{1}$). A simple random mixing model of $(Mn^{2+}, Fe^{2+})SiO_3$ structure was used:

$$G = (G_{MnSiO_3} X_{MnSiO_3} + G_{FeSiO_3} X_{FeSiO_3}) + RT(X_{MnSiO_3} \ln X_{MnSiO_3} + X_{FeSiO_3} \ln X_{FeSiO_3}), \quad [9]$$

where G is the Gibbs energy per formula unit of a solution, G_{MnSiO_3} , G_{FeSiO_3} , X_{MnSiO_3} , and X_{FeSiO_3} are the Gibbs energies and mole fractions of the end-members ($MnSiO_3$ and “ $FeSiO_3$ ”), respectively. This expression is equivalent to assume a Henrian behavior of

“ $FeSiO_3$ ” in the $MnSiO_3$. Since ferrosilite ($FeSiO_3$) is not stable in the Fe-Si-O system at a total pressure of 1 bar, the Gibbs energy of phase transformation of “ $FeSiO_3$ ” from orthopyroxene structure, which is stable at high pressure, to hypothetical rhodonite structure was used as actual model parameter:

$$G_{FeSiO_3(rhodonite)} = G_{FeSiO_3(orthopyroxene)}^\circ + \Delta G_{FeSiO_3}^{orthopyroxene \rightarrow rhodonite}, \quad [10]$$

$G_{FeSiO_3(orthopyroxene)}^\circ$ was taken from Jung *et al.*^[25] and $\Delta G_{FeSiO_3}^{orthopyroxene \rightarrow rhodonite}$ was optimized in the present study. Optimized model parameters are listed in Table II.

D. Braunite

Braunite with “ideal” composition at $3Mn_2O_3 \cdot MnSiO_3$ has solubility toward Mn_2O_3 .^[26,27] The following model structure was considered followed by the suggestion of Abs-Wurmbach^[27]:



in which $[Mn^{2+}Si^{4+}]$ is substituted by two Mn^{3+} ($[Mn^{3+}Mn^{3+}]$) in order to maintain electrical neutrality (coupled substitution).

The Gibbs energy of the braunite solution per formula structure is

$$G = (G_{[MnSi]} X_{[MnSi]} + G_{[MnMn]} X_{[MnMn]}) + RT(X_{[MnSi]} \ln X_{[MnSi]} + X_{[MnMn]} \ln X_{[MnMn]}), \quad [12]$$

where G is the Gibbs energy per formula unit of a solution, $G_{[MnSi]}$, $G_{[MnMn]}$, $X_{[MnSi]}$, and $X_{[MnMn]}$ are the Gibbs energies and mole fractions of the end-members ($3Mn_2O_3 \cdot MnSiO_3$ and “ $3Mn_2O_3 \cdot MnMnO_3$ ”), respectively. As did for the rhodonite solution, since the braunite solution is only stable near $3Mn_2O_3 \cdot MnSiO_3$ composition, the Gibbs energy of phase transformation of “ $3Mn_2O_3 \cdot MnMnO_3$ ” from bixbyite structure to hypothetical braunite structure was used as model parameter:

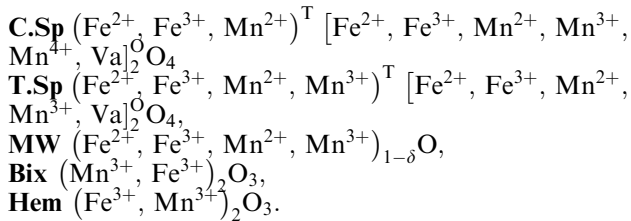
$$G_{[MnMn]} = 4 \times G_{Mn_2O_3(\beta-bixbyite)}^\circ + \Delta G_{[MnMn]}^{\beta-bixbyite \rightarrow braunite}. \quad [13]$$

$G_{Mn_2O_3(\beta-bixbyite)}^\circ$ was taken from Kang and Jung^[6] and $\Delta G_{[MnMn]}^{\beta-bixbyite \rightarrow braunite}$ was optimized in the present study. Optimized model parameters are listed in Table II.

E. Spinel (*C.Sp.*), Tetragonal Spinel (*T.Sp.*), Manganowüstite (*MW.*), Bixbyite (*Bix.*), Hematite (*Hem.*) Solutions

Apart from the above mentioned phases, several solid solutions having distinctive crystal structures and solubility limits are observed in the present FeO- Fe_2O_3 -MnO- Mn_2O_3 - SiO_2 system and listed in Table I. All

these phases were modeled previously using CEF as^[6,8,9]:



Since these phases do not dissolve SiO_2 , there has been no change in models and parameters from the previous studies.^[6,8,9]

The two spinels were modeled separately due to cubic to tetragonal phase transformation.^[6,8,9] Various valence status of iron (Fe^{2+} , Fe^{3+}) and manganese (Mn^{2+} , Mn^{3+} , Mn^{4+}) were considered to be presented in cationic sublattices: tetrahedral site (T) and octahedral site (O). Vacancy was also introduced in the octahedral site in order to model non-stoichiometry toward oxygen-rich composition.

The manganowüstite (also called manganosite when Fe is absent, wüstite when Mn is absent) solution was modeled as a simple random mixture of all cations, Fe^{2+} , Fe^{3+} , Mn^{2+} , and Mn^{3+} ions on cation site using the CEF in one sublattice mixing model. Since the manganowüstite solution does not dissolve appreciable amount of Si, its thermodynamic modeling was taken directly from the present authors' previous work.^[8,9] It was assumed that cation vacancies associate with Fe^{3+} and Mn^{3+} cations in order to maintain electrical neutrality, and do not contribute to the configurational entropy.^[5,6,8,9] The vacancies induce noticeable non-stoichiometry (δ) in the manganowüstite solution, which increases as relative fraction of Fe over Mn increases.^[28–32] As it was reported, the thermodynamic models successfully reproduce the non-stoichiometry reported in the literature.^[28–32]

Bixbyite and hematite phases were modeled as simple Henrian solutions.^[8,9]

The Gibbs energy expression for each phase is similar either to Eq. [4] for spinel and tetragonal spinel, or Eq. [9] for manganowüstite, bixbyite, and hematite. For detailed Gibbs energy expression for each phase, please see the References 6, 8 and 9.

F. Stoichiometric Compound

$\alpha\text{-Mn}_2\text{O}_3$ was treated as a stoichiometric compound in the present study due to limited stability (only at low temperature) resulting no information available.

G. Metallic Phases

All metallic phases (CBCC, CUB, FCC, BCC, Liq.) were treated as simple substitutional solutions and their Gibbs energies of mixing were taken from SGTE database.^[33]

H. Magnetic Properties

Magnetic properties, when observed, in several phases in Fe-O, Mn-O and Fe-Mn, Fe-Mn-O systems

were already modeled and were taken into account.^[5,6,8,9,33]

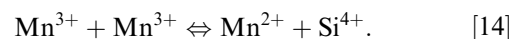
III. CRITICAL EVALUATIONS OF EXPERIMENTAL DATA AND THERMODYNAMIC OPTIMIZATIONS

A. MnO-Mn₂O₃-SiO₂ System

Critical evaluations and thermodynamic modeling/optimizations for the Mn-O and the MnO-SiO₂ system (Mn-Si-O system under reducing gas atmosphere) were well established.^[6,11]

1. Braunite

Muan is probably the first who investigated phase relations in the MnO-Mn₂O₃-SiO₂ system under “controlled” atmosphere. He employed equilibration/quenching followed by X-ray and microscopic method coupled with wet chemical analysis.^[34] He extended this investigation under various “oxidizing” conditions ($p_{\text{O}_2} = 10^{-2.5} - 1$ atm).^[35] Obtained phase equilibria under air in this system are shown in Figure 7. Contrary to the phase diagram of the known MnO-SiO₂ system (Figure 2), rhodonite (MnSiO_3) undergoes a eutectoid reaction at ~ 1321 K (1048 °C), and tephroite (Mn_2SiO_4) is stable only within ~ 26 K. In particular, he reported a wide solubility of SiO_2 in Mn_2O_3 up to ~ 40 mass pct, being a solid solution $\text{Mn}^{2+}(\text{Mn}^{4+}, \text{Si}^{4+})\text{O}_3$, although he left the question open as to the exact nature of the solid solution. Later, this solid solution was revealed as braunite by Abs-Wurmbach.^[26] He investigated stability limit of the braunite ($\text{Mn}_7\text{SiO}_{12}$) using lattice parameter measurement of sample annealed at elevated temperature in air.^[26,27] He observed excess Mn_2O_3 as much as 5 to 10 mass pct and excess MnSiO_3 as much as 2 mass pct in “ideal” braunite ($3\text{Mn}_2\text{O}_3 \cdot \text{MnSiO}_3$). He suggested the following coupled cation substitution in the braunite:



De Villiers and Herstein^[36] reported another type of braunite with SiO_2 -deficiency having a formula $7\text{Mn}_2\text{O}_3 \cdot \text{MnSiO}_3$ which they called “braunite-II.” However, the existence of this phase was rejected by Abs-Wurmbach^[26] who claimed that no super structure reflections belonging to braunite-II was observed in X-ray diffraction pattern of his sample. On the other hand, he always obtained manganese oxide in addition to braunite. In the present study, only the braunite solid solution with the solubility of excess Mn_2O_3 was considered.

Robie *et al.*^[37] measured low-temperature heat capacity of $\text{Mn}_7\text{SiO}_{12}$ using adiabatic calorimetry from 6 K (-267 °C) to 350 K (77 °C), and evaluated molar entropy at 298 K (25 °C) to be 416.4 ± 0.8 J/mol K. This value (416.4 J/mol K) was directly taken in the present study for $S_{298\text{K}}^\circ$. He also employed differential scanning calorimetry in order to measure heat capacity of the $\text{Mn}_7\text{SiO}_{12}$ up to 900 K (627 °C). These data are

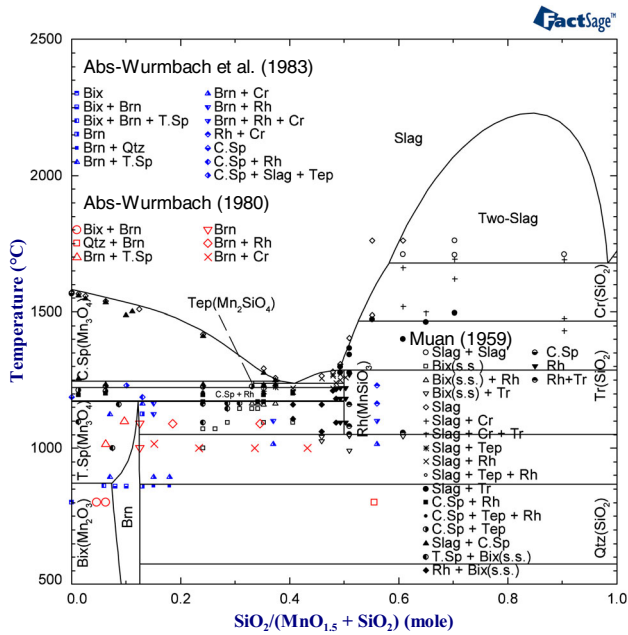


Fig. 7—Optimized phase diagram of the MnO-Mn₂O₃-SiO₂ system in air along with experimental data.^[26,27,34] Legend: Bix: Mn₂O₃ s.s., Brn: Mn₇SiO₁₂ s.s., T.Sp: low temperature α -Mn₃O₄, C.Sp: high temperature β -Mn₃O₄, Qtz: SiO₂ (quartz), Tr: SiO₂ (tridymite), Cr: SiO₂ (cristobalite), Rh: MnSiO₃, Tep: Mn₂SiO₄.

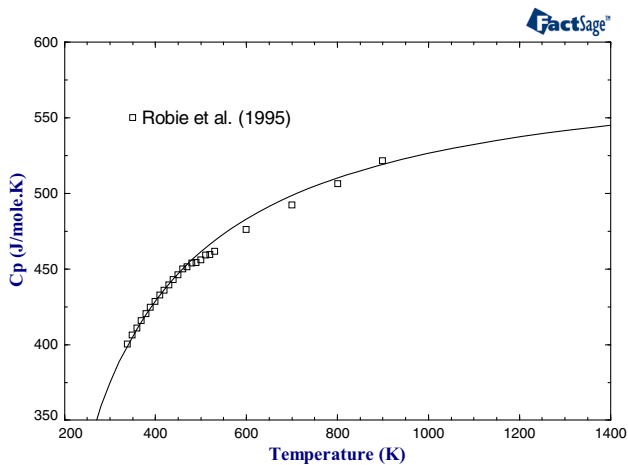


Fig. 8—Optimized heat capacity of braunite (Mn₇SiO₁₂) along with calorimetric data by Robie *et al.*^[37]

shown in Figure 8 along with optimized heat capacity in the present study.

Huang and Rosén^[38] measured equilibrium oxygen partial pressure of Mn₇SiO₁₂ in equilibrium with MnSiO₃ and SiO₂ using EMF technique. Their measured data are shown in Figure 9, and calculated equilibrium oxygen partial pressure is also shown. The calculated oxygen partial pressure is somewhat lower than measured pressure. However, any attempt to reproduce these data would make overall agreement worse in phase equilibria which will be discussed below.

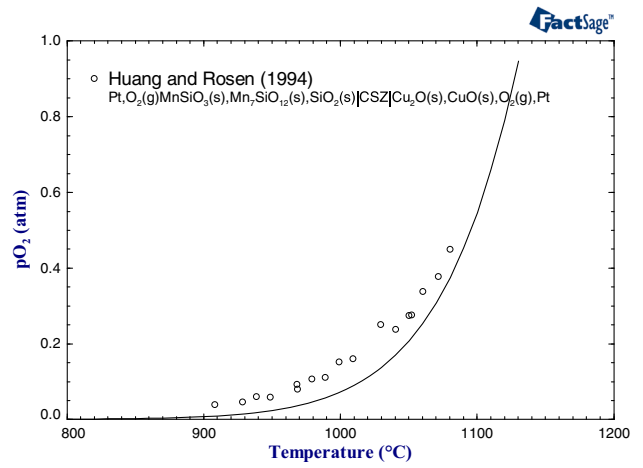


Fig. 9—Equilibrium oxygen partial pressure of Mn₇SiO₁₂ + MnSiO₃ + SiO₂ measured by Huang and Rosén^[38] using EMF technique. Line is calculated from the present study.

2. Phase equilibria in oxidizing condition

Experimental phase equilibria of Muan,^[34] Abs-Wurmbach,^[26] and Abs-Wurmbach *et al.*^[27] are shown together in Figure 7 along with the calculated (optimized) phase diagram in the present study. Tephroite and rhodonite were treated as stoichiometric compounds in this system, although Muan reported little non-stoichiometry of the rhodonite.^[34] Although cristobalite appears even lower temperature than its equilibrium lower limit (1192 K (1465 °C)), it is well known that cristobalite is the phase forming metastably at elevated temperatures prior to tridymite or quartz.^[39] In order to reproduce the liquidus, two model parameters are used in the slag and listed in Table II. Also, $\Delta G_{\text{[MnMn]}^{\beta\text{-bixbyite}\rightarrow\text{braunite}}}$ was optimized in order to reproduce single braunite phase region measured by Abs-Wurmbach.^[27]

Robie *et al.*^[37] estimated enthalpy of formation of the Mn₇SiO₁₂ from both calorimetric and phase equilibrium data (-4260 ± 3.8 kJ/mol). This value was used in the present optimization as an initial value, and finally this was optimized to be -4270 kJ/mol in order to reproduce experimentally determined phase equilibrium data (tetragonal spinel + rhodonite \rightleftharpoons braunite) taking place at 1446 K (1173 °C). This is in good agreement with the measurements of Muan^[34] and Abs-Wurmbach.^[27]

Morris and Muan^[40] investigated liquidus temperature and primary phase of the MnO-Mn₂O₃-SiO₂ slags equilibrated in Pt crucible sealed by silica capsule. Their reported primary phase fields are shown in Figure 10. Lines represent either liquid isotherms or univariant lines of the MnO-Mn₂O₃-SiO₂, calculated by the present model. Since experimental data are available only above 50 mass pct of MnO, and high oxygen pressure ($> \sim 1$ atm) is necessary to reach below this composition limit in practice, the calculation was only carried out in the limited composition area. Agreement between the experiment and the calculation is good except for primary phase field of “Mn₂O₃ s.s. (Bixbyite s.s.)” of Morris and Muan.^[40] As mentioned before, Muan’s observation for the bixbyite s.s.^[34] was rejected by later

Table III. Experimental and Calculated Primary Crystallization Temperatures and Phases in the MnO-Mn₂O₃-SiO₂ System

Composition			Exp. ^[40]		Cal.	
MnO	Mn ₂ O ₃	SiO ₂	T [K (°C)]	Pri. Phase	T [K (°C)]	Pri. Phase
49.3	14.3	36.4	1533 (1260)	Bix	1538.44 (1265.44)	Rh
46	15	39	1539 (1266)	Bix	1562.17 (1289.17)	SiO ₂
69	11	20	1639 (1366)	M	1672.74 (1399.74)	M
68	15	17	1722 (1449)	M	1722.63 (1449.63)	M
65	20	15	1729 (1456)	M	1731.97 (1458.97)	M
62.5	25.5	12	1736 (1463)	M	1760.22 (1487.22)	M
60	30	10	1755 (1482)	M	1772.68 (1499.68)	M
70	22	8	1823 (1550)	M	1867.17 (1594.17)	M
54	9	37	1524 (1251)	Rh	1531.49 (1258.49)	Rh
56.5	5	38.5	1530 (1257)	Rh	1531.79 (1258.79)	Rh
50	12	38	1530 (1257)	Rh	1544.92 (1271.92)	Rh
50	9	41	1534 (1261)	Rh	1550.64 (1277.64)	Rh
54.5	12	33.5	1526 (1253)	C.Sp	1521.55 (1248.55)	C.Sp
57	10	33	1526 (1253)	C.Sp	1533.25 (1260.25)	Tep
52	13	35	1530 (1257)	C.Sp	1523.8 (1250.8)	Rh
65	12	23	1588 (1315)	C.Sp	1616.49 (1343.49)	C.Sp
63	12	25	1598 (1325)	C.Sp	1604.36 (1331.36)	C.Sp
55	15	30	1612 (1339)	C.Sp	1560.88 (1287.88)	C.Sp
65	15	20	1623 (1350)	C.Sp	1648.17 (1375.17)	C.Sp
56	19	25	1656 (1383)	C.Sp	1627.64 (1354.64)	C.Sp
60	18	22	1673 (1400)	C.Sp	1652.52 (1379.52)	C.Sp
61.5	23	15.5	1687 (1414)	C.Sp	1711.97 (1438.97)	C.Sp
60	20	20	1720 (1447)	C.Sp	1675.72 (1402.72)	C.Sp
53	44	3	1803 (1530)	C.Sp	1823.86 (1550.86)	M
49	49	2	1808 (1535)	C.Sp	1830.69 (1557.69)	C.Sp
55.5	9.5	35	1513 (1240)	Tep	1511.13 (1238.13)	C.Sp
58	5	37	1538 (1265)	Tep	1515.99 (1242.99)	Rh
60	11	29	1580 (1307)	Tep	1572.55 (1299.55)	Tep
68	9	23	1588 (1315)	Tep	1597.2 (1324.2)	C.Sp
63	5	32	1593 (1320)	Tep	1575.26 (1302.26)	Tep
65.7	8	26.3	1594 (1321)	Tep	1590.12 (1317.12)	Tep
54.5	10.5	35	1497 (1224)	Tep + Rh	1515.26 (1242.26)	Rh
43	16	41	~1603 (1330)	SiO ₂	1697.3 (1424.3)	SiO ₂
46	13	41	~1623 (1350)	C.Sp	1632.35 (1359.35)	SiO ₂
49	17	34	~1643 (1370)	C.Sp	1519.97 (1246.97)	Rh
47.4	20	32.6	~1643 (1370)	SiO ₂	1528.67 (1255.67)	C.Sp
49	8	43	~1663 (1390)	M	1620.81 (1346.81)	SiO ₂
80	10	10	~1933 (1660)	—	1926.27 (1653.27)	M
57	41	2	<1803 (1530)	—	1851.27 (1578.27)	M
68	32	0	<1822 (1549)	—	1929.38 (1656.38)	M
72	28	0	<1822 (1549)	C.Sp	1953.15 (1680.15)	M
59	41	0	>1826 (1553)	C.Sp	1878.79 (1605.79)	M
64	36	0	>1826 (1553)	—	1906.07 (1633.07)	M

Composition in mass percent. Legend: M: Manganosite, Bix: Mn₂O₃ s.s., C.Sp: high temperature β-Mn₃O₄, Rh: MnSiO₃, Tep: Mn₂SiO₄.

investigations^[26,27] as well as in the present study. Therefore, the observed bixbyite s.s. might be in error, and these two data points were discarded in the present optimization. The two compositions showing bixbyite s.s. as a primary phase field fall into rhodonite primary phase field in the present calculation. Actually, they reported that secondary phase in the two samples was rhodonite. Table III shows comparison of liquidus temperature and primary phase at each composition between the investigation by Morris and Muan^[40] and the present calculation. Calculated invariant temperatures for reactions (1) slag ⇌ manganosite + spinel + tephroite, (2) slag ⇌ rhodonite + spinel + tephroite are 1578 K (1305 °C) and 1509 K (1236 °C), respectively.

These are in good agreement with the reported temperatures 1576 K (1303 °C) and 1493 K (1220 °C).^[40]

B. FeO-Fe₂O₃-MnO-Mn₂O₃-SiO₂ System

Critical evaluation and thermodynamic modeling/optimizations for the Fe-O, FeO-Fe₂O₃-SiO₂, and the FeO-Fe₂O₃-MnO-MnO₂ systems were well established,^[5,8-10] and those of other sub-systems in the present FeO-Fe₂O₃-MnO-Mn₂O₃-SiO₂ system were described in Section III.I.

Calculated liquidus projections of the FeO-Fe₂O₃-MnO-Mn₂O₃-SiO₂ system under reducing

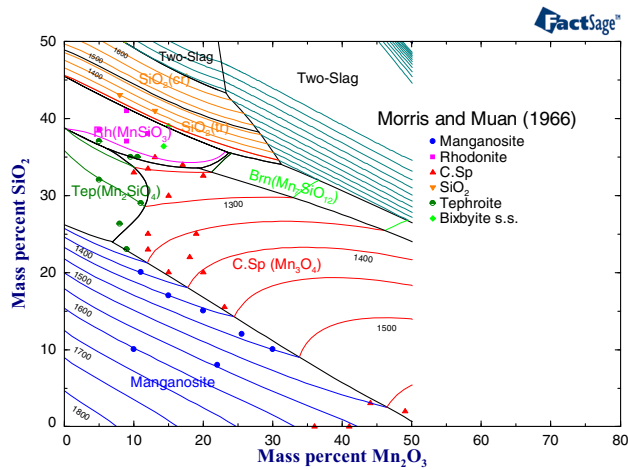


Fig. 10—Calculated (part of) liquidus surface of the MnO-Mn₂O₃-SiO₂ system (temperature in °C). Experimental data were taken from Morris and Muan.^[40]

condition (metallic Fe saturation) and under oxidizing condition (in air) are shown in Figure 11. The liquidus projection under reducing condition (Figure 11(a)) is governed mostly by primary phase fields of manganowüstite, olivine, and immiscible two slags. Primary phase of rhodonite is terminated by those of tridymite and olivine because ferrosilite (FeSiO₃) is not stable in the Fe-Si-O system at a total pressure of 1 atm. Manganowüstite extends from manganosite (MnO) to wüstite (Fe_{1-x}O). On the other hand, in air, the manganowüstite transforms to (cubic) spinel extending β -hausmanite (β -Mn₃O₄) to magnetite (Fe₃O₄). Primary phase fields of this spinel and immiscible two slags occupy most part of the liquidus surface in air, as shown in Figure 11(b). Although rhodonite and tephroite, both of which contain divalent Mn, persist in this oxidizing atmosphere, their primary phase fields shrink dramatically.

Many types of experimental data are available in the present FeO-Fe₂O₃-MnO-Mn₂O₃-SiO₂ system, such as phase equilibria, thermodynamic data, and structural data. All these data were evaluated, and reliable data were used in the optimization of model parameters.

1. Structural data in olivine

As already mentioned, olivine has two distinctive cationic sublattices, namely M1 and M2. Since size of M2 site is larger than that of M1 site, cationic ordering occurs that larger cation (Mn²⁺) prefers to enter in the larger M2 site. This tendency becomes weak, however, as temperature increases due to thermal motion of cations. In Figure 12, two sets of experimentally determined structural data of (Fe, Mn)SiO₄ are shown. Redfern and co-workers^[41–44] employed *in situ* neutron diffraction method to measure cation distribution in the olivine from room temperature to 1273 K (1000 °C). They measured the cation distribution in heating cycle and cooling cycle both, and observed that cations do not reach their equilibrium position at low temperature (<~823 K (550 °C)). Another investigation by the same

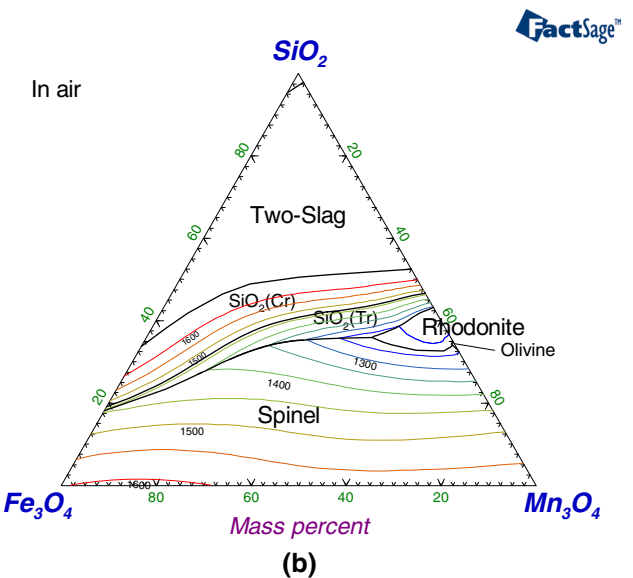
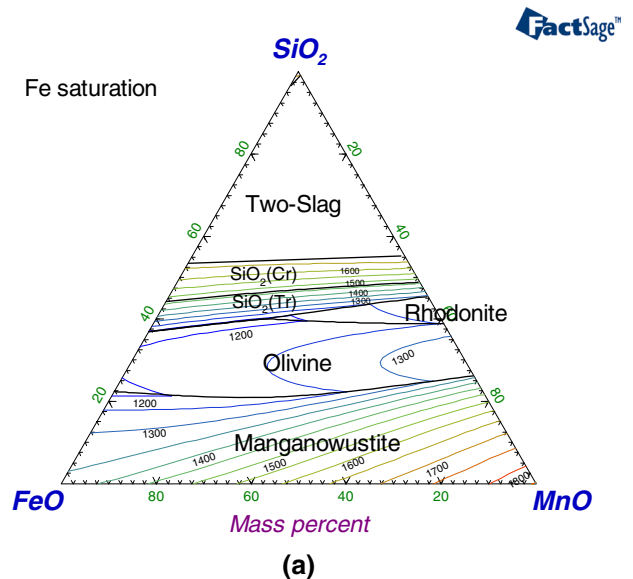


Fig. 11—Optimized liquidus surfaces of the FeO-Fe₂O₃-MnO-Mn₂O₃-SiO₂ system (temperature in °C). (a) Equilibrium with metallic Fe and (b) in air.

authors^[45] is also shown by open symbols. This investigation employed neutron diffraction technique with samples annealed at 1423 K (1150 °C) followed by quenching. These two sets of cationic fraction data differ significantly; however, the reason is not clear at present. Since their first investigation^[41–44] employed *in situ* technique over wide range of temperature, these data were taken into account in the present study in order to optimize the parameter I_{FM} . Only the cation distribution data above ~723 K (550 °C) were considered being true equilibrium data. As shown in the figure, the optimized cationic fraction of Mn in M2 site is in good agreement with the experimental data above ~723 K (550 °C). Figure 13 shows calculated cationic fractions of Fe²⁺ in M1 and M2 sites at 1273 K (1000 °C) and 1323 K (1150 °C), along with experimental data of Annersten *et al.*^[46] at 1323 K (1000 °C), Redfern *et al.*^[45] at 1323 K

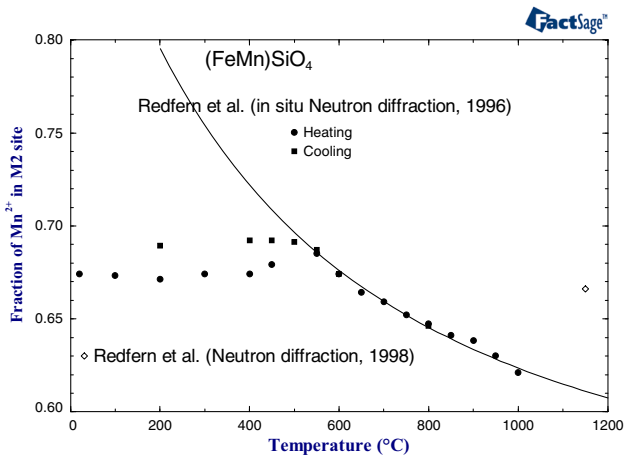


Fig. 12—Cation distribution (site fraction of Mn in M2 site) of olivine $(\text{Fe}_{0.5}\text{Mn}_{0.5})_2\text{SiO}_4$ as function of temperature.^[41–45] Line is calculated in the present study. Experimental data below ~ 823 K (550°C) seem not to reach true equilibrium due to low thermal energy.^[41–44]

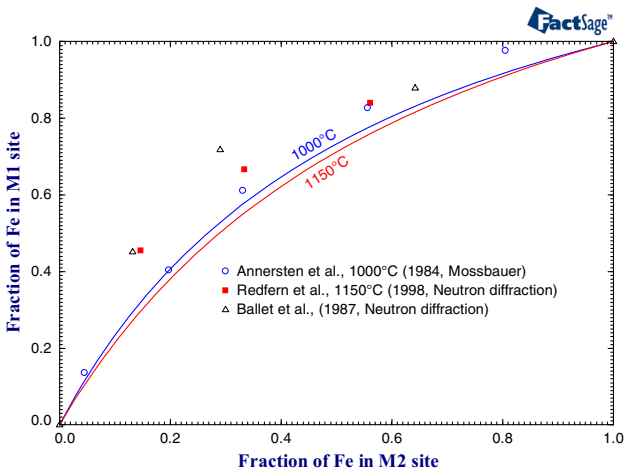


Fig. 13—Cation distribution (site fractions of Fe^{2+} in M2 and M1 sites) of olivine $(\text{Fe, Mn})_2\text{SiO}_4$.^[45–47] Lines are calculated at 1273 K (1000°C) and 1423 K (1150°C).

(1150°C) (in the same investigation shown in Figure 12), and Ballet *et al.*^[47] at unknown temperature. The calculated cation distribution at 1273 K (1000°C) shows good agreement with the data of Annersten *et al.*^[46] If the discrepancy of Redfern *et al.*'s data^[45] is taken into account as shown in Figure 12, the calculation at 1323 K (1150°C) may be acceptable.

2. Solid–solid equilibrium under reducing condition

An isothermal section under reducing condition (metallic alloys saturation) showing sub-solidus phase equilibria was calculated at 1323 K (1150°C), and it is shown in Figure 14. There are several two-oxide and three-oxide equilibria under this condition. Schwerdtfeger and Muan^[48] measured solid phase equilibria under various oxygen partial pressures, using either equilibration/quenching coupled with microscopic/

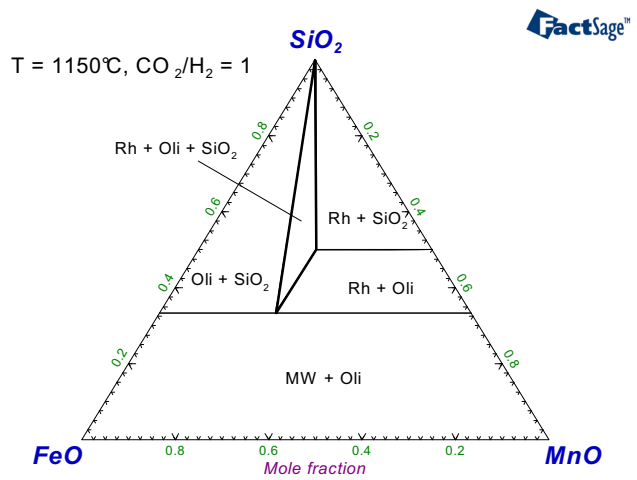


Fig. 14—Calculated isothermal section of the $\text{FeO-Fe}_2\text{O}_3\text{-MnO-Mn}_2\text{O}_3\text{-SiO}_2$ system at 1423 K (1150°C) under $p_{\text{CO}_2}/p_{\text{H}_2} = 1$. Legend: MW: magnesiowüstite, Oli: olivine, Rh: Rhodonite.

XRD or thermogravimetric method at 1323 K (1150°C). These results are shown in Figure 15. Calculated equilibrium oxygen partial pressures shown as lines are in good agreement with the experimental data within error limits. It may be noted that equilibrium oxygen partial pressures in same phase equilibria (olivine + rhodonite + FCC + gas) are shown in Figures 15(b) and (c), but these were measured from different samples and expressed as function of composition in olivine (Figure 15(b)) and in rhodonite (Figure 15(c)), respectively.

They also measured tie lines between manganowüstite and olivine under $p_{\text{CO}}/p_{\text{CO}_2} = 2.5$ at 1323 K (1150°C). Compositions of each phase were derived from d spacings measurement using XRD. These data are shown in Figure 16 with the calculated equilibrium compositions of the two-phase under the same condition. As pointed out by the authors, d spacings of olivine phase by X-ray vary somewhat less with composition than that of manganowüstite phase does. With this consideration, the agreement between the measurement and the calculation seems quiet reasonable.

These types of calculations are practically very important in the prediction of oxide scale forming on various grades of steels in annealing furnace.^[49] Depending on temperature, steel chemistry, and dew point (oxygen partial pressure), different kinds of phases are formed as the scale. Types of phases formed on the steel surface govern hot-dip galvanizing performance.^[50]

For the Fe-Mn olivine, no excess Gibbs energy parameter was required, contrary to Ca-Fe olivine^[51] and Ca-Mn olivine^[52] which required positive excess energies in order to form low temperature miscibility gap.

3. Activities in slags

Activities of “FeO” and MnO in $\text{Fe}_t\text{O-MnO-SiO}_2$ slags were measured in several investigations, mostly in equilibrium with either solid $\text{Fe}^{[53]}$ or liquid $\text{Fe}^{[54]}$ Some

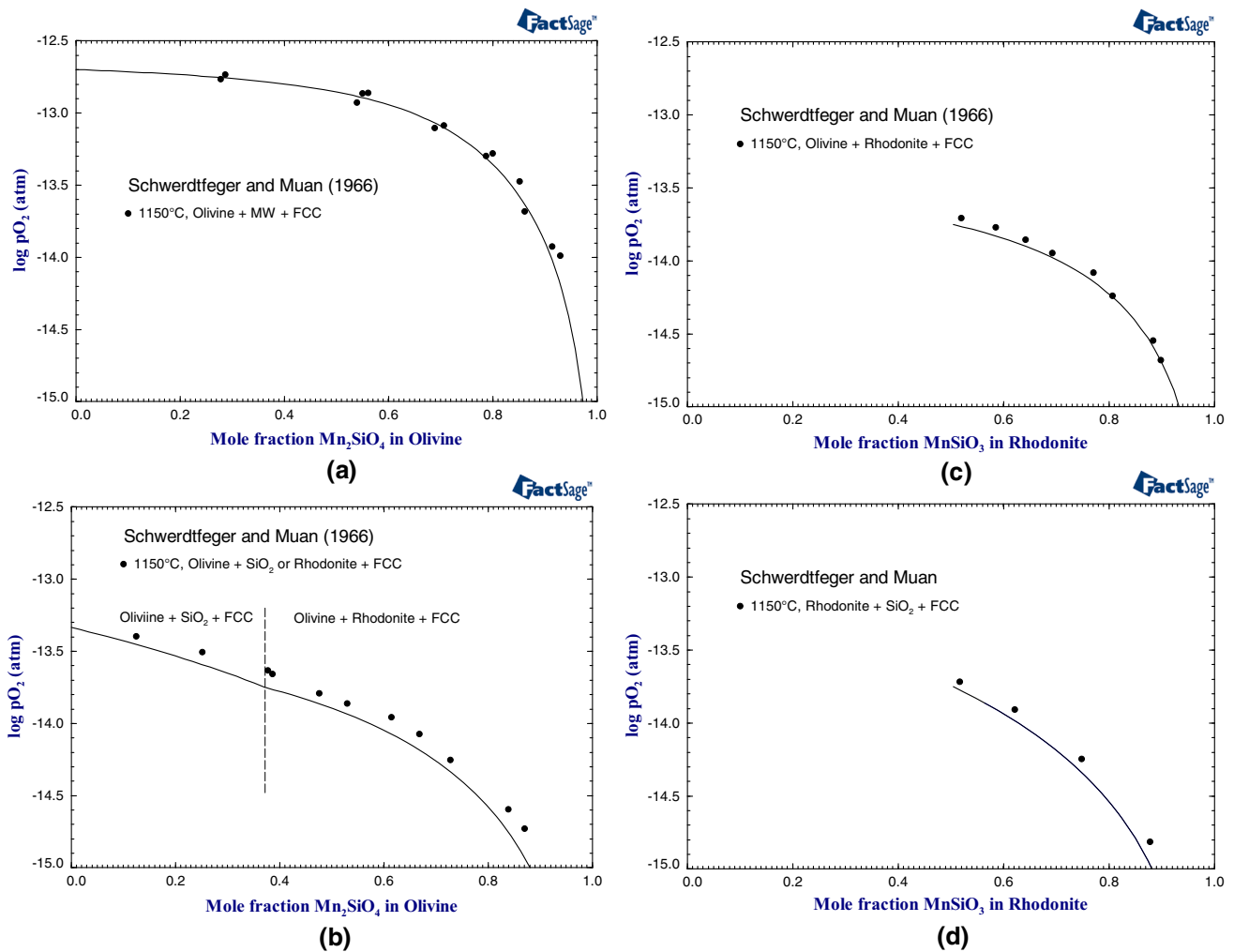


Fig. 15—Equilibrium oxygen partial pressures of phase assembly of (a) olivine + manganowüstite + FCC, (b) olivine + SiO₂ or rhodonite + FCC, (c) olivine + rhodonite + FCC, and (d) rhodonite + SiO₂ + FCC, at 1423 K (1150 °C). Experimental data were taken from Schwerdtfeger and Muan.^[48]

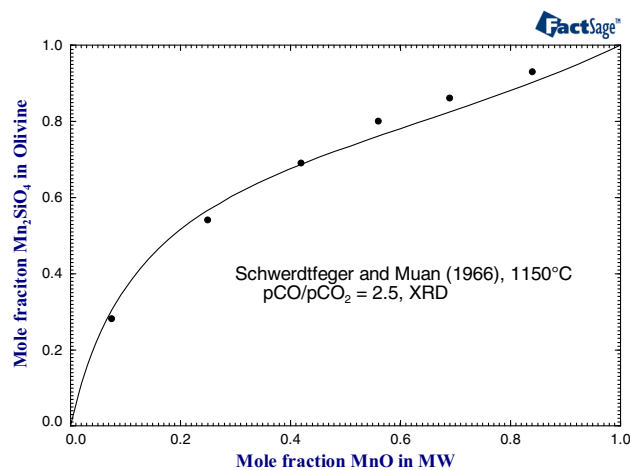
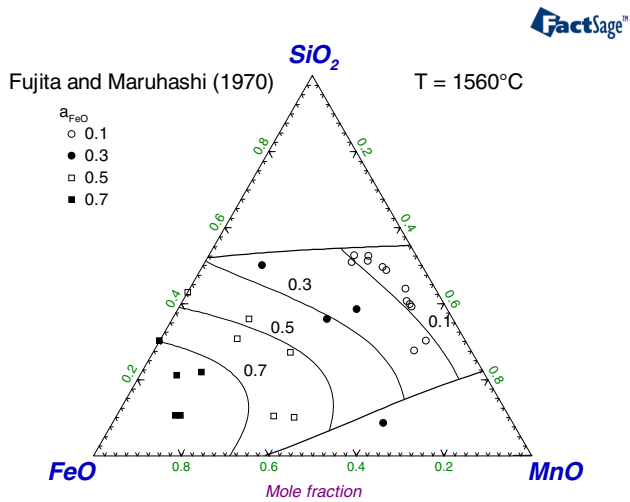


Fig. 16—Tie-line between manganowüstite (MW) and olivine under $p_{\text{CO}}/p_{\text{CO}_2} = 2.5$ at 1423 K (1150 °C).^[48] Line is calculated in the present study.

measurements were conducted in liquid Fe and silica co-saturation condition.^[54–57] With known activity coefficients of Mn, Si, and O in molten Fe, activities of component in slags were calculated by the authors. Figures 17 and 18 show experimentally determined activity of “FeO” and MnO, respectively. Reference state of “FeO” is defined as pure liquid iron oxide in equilibrium with pure iron, and that of MnO is pure manganese oxide. Also shown in the figures are the calculated iso-activity lines of “FeO” and MnO (and saturation boundary of SiO₂ and manganowüstite). The calculations in the present study are in good agreement with the data of Ban-Ya *et al.*^[53] Also, the data of Fujita and Maruhashi *et al.*^[54] were fairly well reproduced within experimental scatters as shown in the figures.

Figure 19 shows the calculated activity of “FeO” (as function of mole fraction of FeO) and MnO (as function of mole fraction of MnO) in Fe₁O-MnO-SiO₂ slags saturated by SiO₂ and Fe. Also the same reference states to those used in Figures 17 and 18 were used. Experimentally determined activities at various compositions



(a)

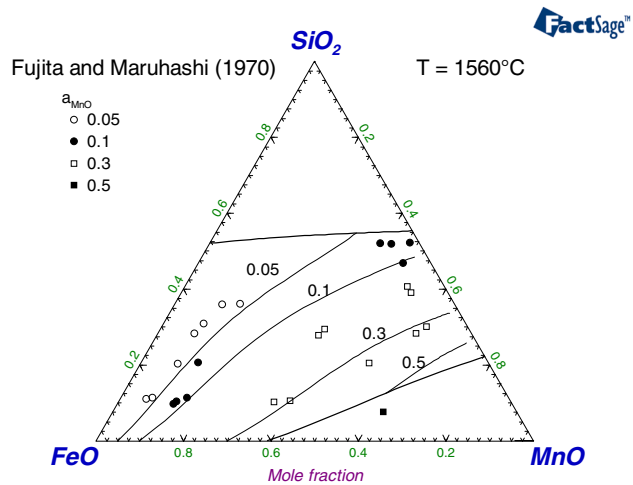
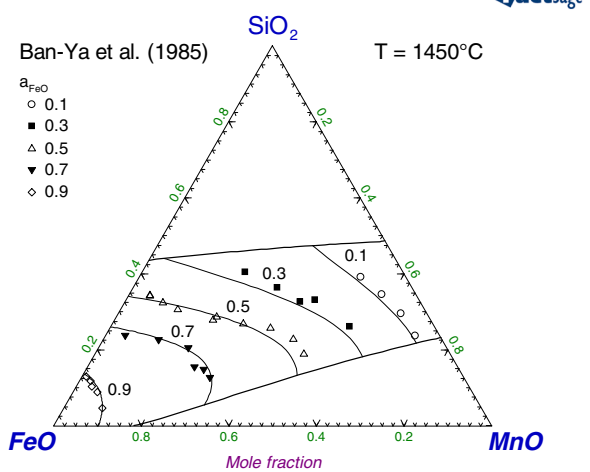


Fig. 18—Activity of MnO (with respect to pure liquid MnO) in $\text{Fe}_t\text{O-MnO-SiO}_2$ slag in equilibrium with metallic Fe at $T = 1833 \text{ K}$ (1560°C).^[54] Lines are calculated iso-activity lines (thin line) and phase boundaries (thick lines) in the present study.



(b)

Fig. 17—Activity of “FeO” (with respect to pure liquid Fe oxide in equilibrium with pure Fe) in $\text{Fe}_t\text{O-MnO-SiO}_2$ slag in equilibrium with metallic Fe at (a) $T = 1833 \text{ K}$ (1560°C)^[54] and (b) $T = 1723 \text{ K}$ (1450°C).^[53] Lines are calculated iso-activity lines (thin lines) and phase boundaries (thick lines) in the present study.

and temperatures are also shown for comparison. The calculations reproduce the measured activity well. It can be seen that there is almost negligible dependence on temperature, either from the experiments or from the calculations in the present study. This is due to very steep liquidus of SiO_2 in this slag retaining almost similar liquidus compositions (as shown in Figure 11(a)).

4. Phase diagrams

Riboud and Muan^[58] determined liquidus and solidus of two sections ($X_{\text{SiO}_2} = 1/3$, and mass pct of $\text{SiO}_2 = 38$ to 44) under “reducing” (but not specified explicitly) gas atmosphere ($\text{CO}_2 + \text{H}_2$ inlet mixture) using equilibration/quenching followed by X-ray diffraction and microscopic analysis. They stated that “the mixing ratios were chosen such that wüstite (‘FeO’) was the stable phase of iron oxide. Under these conditions, MnO

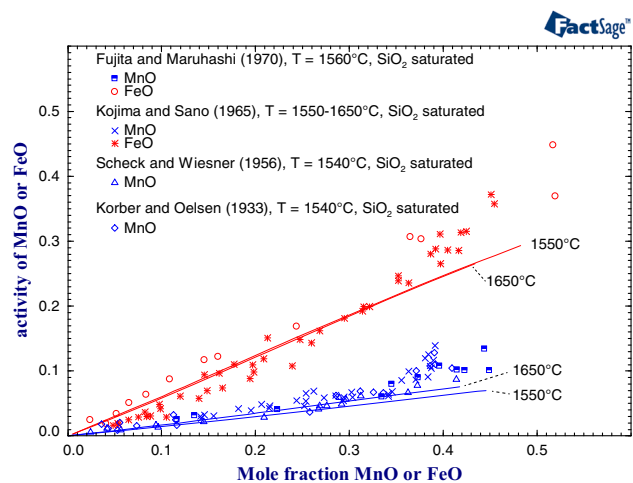


Fig. 19—Activity of “FeO” (with mole fraction FeO) and MnO (with mole fraction MnO) in $\text{Fe}_t\text{O-MnO-SiO}_2$ slag in equilibrium with metallic Fe in the temperature range 1813 K (1540°C) to 1923 K (1650°C) at SiO_2 saturation.^[54–57] Lines are calculated in the present study. Standard states for each component are the same to those in Figures 17 and 18.

and silicates of divalent iron and manganese are also stable”.^[58] Probably, this atmosphere might be close to metallic Fe saturation, and in the present study, their experimental work was compared to the calculation under the metallic Fe saturation condition. Figure 20 shows calculated phase diagram sections ($X_{\text{SiO}_2} = 1/3$, and mass pct of $\text{SiO}_2 = 40$) at metallic Fe saturation, along with the experimental data measured by Riboud and Muan.^[58] Calculated phase diagram in two sections are in good agreement with the measured phase equilibria. Although Figure 20(a) lies in metasilicate section of “FeO”-MnO- SiO_2 sub-system, rhodonite phase is always saturated by olivine or slag due to metallic Fe saturation condition. On the other hand, Figure 20(b) lies between metasilicate and orthosilicate sections, and

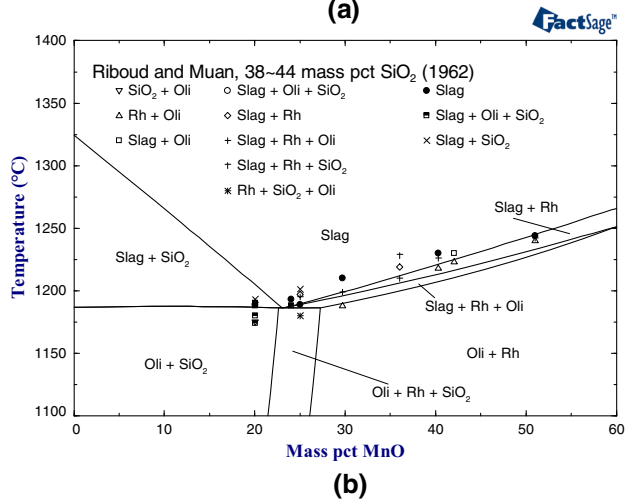
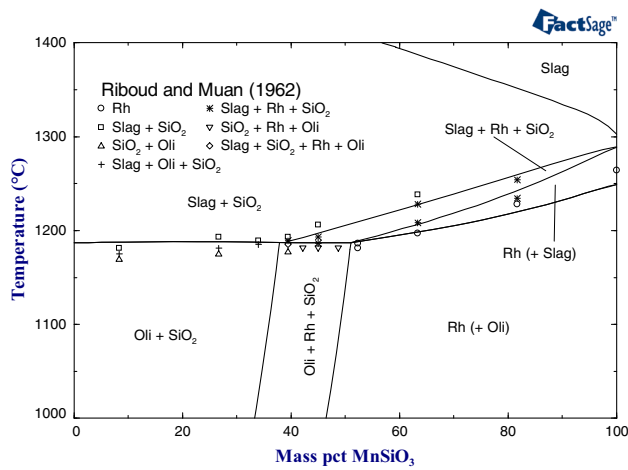


Fig. 20—Optimized phase diagram sections along (a) $\text{Fe}_2\text{SiO}_4\text{-MnSiO}_3$ and (b) 40 mass pct SiO_2 ($=\text{SiO}_2/(\text{FeO} + \text{MnO} + \text{SiO}_2)$) in the $\text{FeO-Fe}_2\text{O}_3\text{-MnO-Mn}_2\text{O}_3\text{-SiO}_2$ system at metallic Fe saturation. Experimental data were taken from Riboud and Muan.^[58] Phase names in parentheses represent the phases in very low phase fraction (usually less than 1 pct). Legend: Oli: olivine, Rh: Rhodonite.

the rhodonite + olivine two-phase equilibrium actually appears.

There have been a number of measurements on liquidus temperatures in orthosilicate section of the “FeO”-MnO-SiO₂ system. However, earlier investigations^[59–61] showed improbable liquidus shape having one or two minima of along liquidus. From the consideration that olivine forms a continuous solid solution from Fe_2SiO_4 to Mn_2SiO_4 ,^[58] this cannot be accepted. Later, Carter *et al.*^[62] determined liquidus and solidus temperatures of the orthosilicate section. They used iron crucible and observed beginning and end of melting by means of low-power microscope under oxygen-free nitrogen atmosphere. Their measured liquidus points did not show any minimum, but their measured liquidus and solidus temperature were not conclusive in the author’s own opinion due to difficulty encountered during measurement. Therefore, their data were not considered as true equilibrium data. Figure 21 shows calculated phase diagram of the orthosilicate

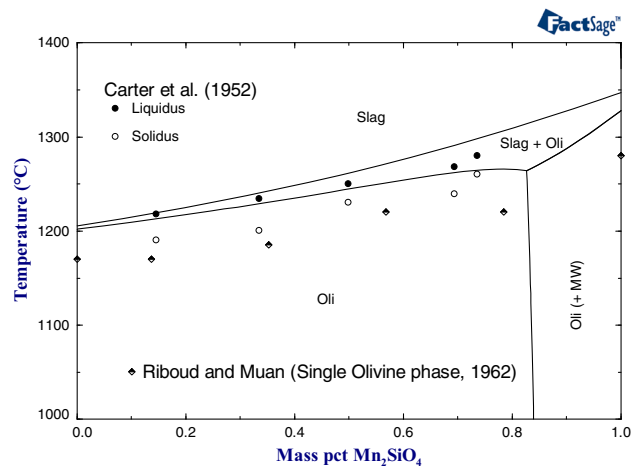


Fig. 21—Optimized phase diagram section along $\text{Fe}_2\text{SiO}_4\text{-Mn}_2\text{SiO}_4$ in the $\text{FeO-Fe}_2\text{O}_3\text{-MnO-Mn}_2\text{O}_3\text{-SiO}_2$ system at metallic Fe saturation. Experimental data were taken from Carter *et al.*,^[62] and Riboud and Muan.^[58] Phase names in parentheses represent the phases in very low phase fraction (usually less than 1 pct). Legend: Oli: olivine, MW: magnesiowüstite.

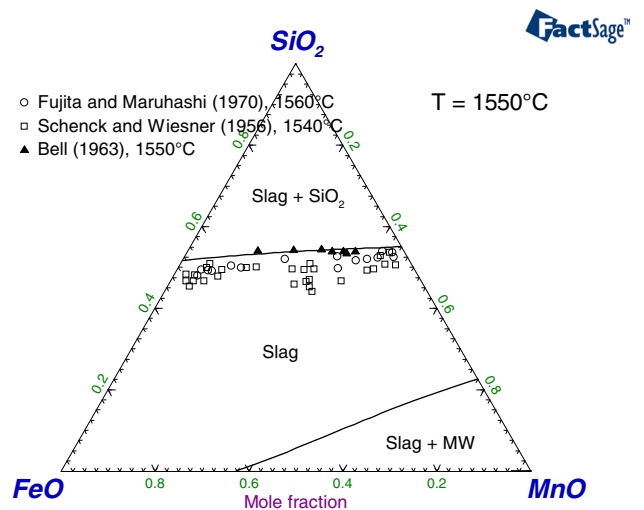


Fig. 22—Calculated liquidus of SiO_2 in FeO-MnO-SiO_2 slag in equilibrium with metallic Fe at 1823 K (1550 °C) along with experimental data.^[54,56,63]

section of the “FeO”-MnO-SiO₂ system in metallic Fe saturation. Experimental data of single olivine phase confirmed by Riboud and Muan^[58] are also plotted. As was seen before for the metasilicate section, although Figure 21 lies on orthosilicate section of “FeO”-MnO-SiO₂ sub-system, manganese-rich olivine phase is saturated by manganowüstite due to metallic Fe saturation condition. This calculated phase diagram (liquidus and solidus) is believed to be close to reality; however, further experimental investigation in this section is required in order to either confirm or refine the present thermodynamic modeling.

SiO_2 liquidus (slag composition saturated by silica) was measured at 1813 K (1540 °C) to 1833 K (1560 °C) by several authors.^[54,56,63] The calculated SiO_2 liquidus

Table IV. Invariant Reactions in the FeO-Fe₂O₃-MnO-Mn₂O₃-SiO₂ System

Reaction	T [K (°C)], Exp.	T [K (°C), Cal.	Note
Slag + Rh ⇌ SiO ₂ (Tr) + Oli	1731 ± 5 (1458 ± 5) ^{[58]†}	1732 (1459)	In equil. with Fe
Slag ⇌ SiO ₂ (Tr) + Rh + C.Sp	1478 (1205) ^{[65]†}	1479 (1206)	In air
Slag ⇌ Oli + Rh + C.Sp	1478 (1205) ^{[65]†}	1508 (1235) [‡]	In air
Slag ⇌ Rh + C.Sp (max.) [§]	1493 (1220) ^{[65]†}	1509 (1236) [‡]	In air

[‡] In an atmosphere of $p_{CO_2}/p_{H_2} = 1$.

[†] See text for the reason of discrepancy between experiment and calculation.

[§] This is not an invariant reaction but a maximum along univariant line between spinel and rhodonite.

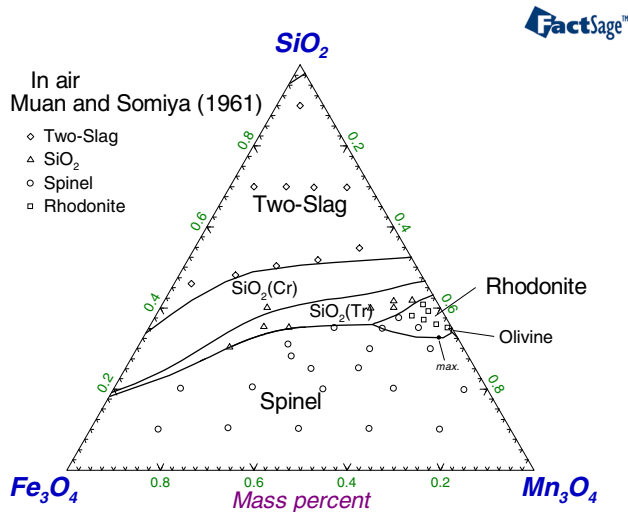


Fig. 23—Calculated primary phase fields in FeO-Fe₂O₃-MnO-Mn₂O₃-SiO₂ in air. Experimental data were taken from Muan and Somiya.^[65]

at 1823 K (1550 °C) is shown in Figure 22 along with the experimental data. The present calculation is in excellent agreement with the data of Bell^[63] at the same temperature. Two other measurements show lower SiO₂ contents in slags. These measurements cannot be accounted for by the present model because they are not consistent even with the SiO₂ liquidus in “FeO”-SiO₂ and MnO-SiO₂ binary systems. In order to reproduce these phase diagram data as well as the activity data, one small ternary parameter for slag in reducing condition was introduced (See Table II).

Based on measurement of liquidus shown in Figure 20, Riboud and Muan^[58] and Muan and Osborn^[64] estimated liquidus projection of the FeO-Fe₂O₃-MnO-Mn₂O₃-SiO₂ system in reducing condition ($p_{CO_2}/p_{H_2} = 1$). Their liquidus projection is actually almost identical to the calculated liquidus projection shown in Figure 11(a). One invariant reaction was reported at 1458 ± 5 K (1185 ± 5 °C)^[58] and this is in excellent agreement with the calculated invariant temperature at 1459 K (1186 °C; see Table IV).

Experimental investigation under oxidizing condition is very rare. The only experimental work found was due to Muan and Somiya^[65] who employed equilibration (in air)/quenching followed by microscopic and X-ray analysis. Unfortunately, they did not provide actual experimental data in their publication.^[65] Only

information available was about primary phase field, and estimated liquidus projection with invariant points. Nevertheless, using these information, one ternary parameter was optimized for slag in oxidizing condition in order to reproduce the data (see Table II). Figure 23 shows a comparison of primary phase fields in FeO-Fe₂O₃-MnO-Mn₂O₃-SiO₂ system in air between the experiment^[65] and the calculation in the present study. Except for the univariant line between spinel and rhodonite which differs by about 4 to 6 mass pct, generally good agreement was obtained.

They reported three invariant reactions and the reported temperatures were compared in Table IV. A eutectic temperature involving rhodonite, spinel, and tridymite is in excellent agreement with each other (1478 K (1205 °C) from experiment vs 1479 K (1206 °C) from the present calculation). However, temperatures of two other reactions differ as much as 16 to 30 K. It should be noticed that these two reactions take place very close to the Mn₃O₄-SiO₂ edge, as shown in Figure 23. In 1959, Muan published his phase diagram study of manganese oxide-silica in air,^[34] and he reported the lowest temperature involving slag (slag ⇌ tephroite + rhodonite) to be 1479 K (1206 °C). However, in a later publication in 1966 with Morris,^[40] Muan corrected this temperature to be ≥1493 K (1220 °C), and noted that there were “difficulties of distinguishing tephroite crystals formed below and above solidus temperature”.^[40] This implies that the investigation by Muan and Somiya^[65] near Mn₃O₄-SiO₂ edge in the iron-manganese silicate might estimate these temperatures lower than true equilibria. Therefore, the two invariant reactions reported by Muan and Somiya might be in error, if they estimated these temperatures based on his earlier measurement in 1959 in Mn₃O₄-SiO₂ system.^[34] If a rough correction to their temperatures for these two reactions were made by increasing them as much as 15 K (difference between their old and new eutectic temperatures in the MnO-Mn₂O₃-SiO₂ system in air, namely, 1479 K (1206 °C) and ≥1493 K (1220 °C), respectively), then the two temperatures would be closer to the present calculations giving maximum difference of 15 K.

IV. CONCLUSION

Critical evaluations and thermodynamic optimizations for the MnO-Mn₂O₃-SiO₂ system and FeO-Fe₂O₃-MnO-Mn₂O₃-SiO₂ system were performed in the present study. The optimized model parameters

can reproduce all reliable thermodynamic and structural data as well as the phase diagrams of the FeO-Fe₂O₃-MnO-Mn₂O₃-SiO₂ system within experimental error limits. The database of model parameters can be used with general thermodynamic software, such as FactSage,^[15-17] in order to calculate the thermodynamic properties such as activity, and phase equilibria as functions of temperatures, compositions, and oxygen partial pressures where experimental data are not available. This system is of particular importance to represent oxide scale on various steel grades.^[49]

REFERENCES

1. Y.-B. Kang and H.-G. Lee: *ISIJ Int.*, 2004, vol. 44, pp. 1006–15.
2. I.-H. Jung, S. Deckerov, and A.D. Pelton: *ISIJ Int.*, 2004, vol. 44, pp. 527–36.
3. Y. Gong, H.-S. Kim, and B.C. de Cooman: *ISIJ Int.*, 2008, vol. 48, pp. 1745–51.
4. Y. Gong, H.-S. Kim, and B.C. de Cooman: *ISIJ Int.*, 2009, vol. 49, pp. 557–63.
5. S. Degterov, E. Jak, P. Hayes, and A. Pelton: *Metall. Mater. Trans. B.*, 2001, vol. 32B, pp. 643–57.
6. Y.-B. Kang and I.-H. Jung: *Metall. Mater. Trans. E.*, 2016, vol. 3E, pp. 156–70.
7. P. Wu, G. Eriksson, and A. Pelton: *J. Am. Ceram. Soc.*, 1993, vol. 76, pp. 2065–75.
8. Y.-B. Kang and I.-H. Jung: *J. Phys. Chem. Solids*, 2016, vol. 98, pp. 237–46.
9. Y.-B. Kang and I.-H. Jung: *J. Phys. Chem. Solids*, 2017, vol. 101, p. 90.
10. E. Jak, P. Hayes, A. Pelton, and S. Deckerov: *Int. J. Mater. Res.* (formerly *Z. Metallkd.*), 2007, vol. 98, pp. 847–54.
11. G. Eriksson, P. Wu, M. Blander, and A. Pelton: *Can. Metall. Q.*, 1994, vol. 33, pp. 13–22.
12. A. Pelton and M. Blander: *Proc. 2nd Int. Symp. Metall. Slags Fluxes*, TMS-AIME, Warrendale, PA, 1984, pp. 281–94.
13. A. Pelton and M. Blander: *Metall. Trans. B.*, 1986, vol. 17B, pp. 805–15.
14. A. Pelton, S. Degterov, G. Eriksson, C. Robelin, and Y. Dessureault: *Metall. Mater. Trans. B.*, 2000, vol. 31B, pp. 651–59.
15. C. Bale, P. Chartrand, S. Degterov, G. Eriksson, K. Hack, R.B. Mahfoud, J. Melançon, A. Pelton, and S. Petersen: *Calphad*, 2002, vol. 26, pp. 189–228.
16. C. Bale, É. Belisle, P. Chartrand, S. Degterov, G. Eriksson, K. Hack, I.-H. Jung, Y.-B. Kang, J. Melançon, A. Pelton, C. Robelin, and S. Petersen: *Calphad*, 2009, vol. 33, pp. 295–311.
17. C. Bale, É. Belisle, P. Chartrand, S. Degterov, G. Eriksson, A. Gheribi, K. Hack, I.-H. Jung, Y.-B. Kang, J. Melançon, A. Pelton, S. Petersen, C. Robelin, J. Sangster, P. Spencer, and M.-A. Van Ende: *Calphad*, 2016, vol. 54, pp. 35–53.
18. A. Pelton and P. Chartrand: *Metall. Mater. Trans. A.*, 2001, vol. 32A, pp. 1355–60.
19. G. Eriksson and A.D. Pelton: *Metall. Trans. B.*, 1993, vol. 24B, pp. 807–16.
20. A. Pelton: *Calphad*, 2001, vol. 25, pp. 319–28.
21. W. Deer, R. Howie, and J. Zussman: *An Introduction to the Rock-Forming Minerals*, 2nd ed., Addison-Wesley Pub. Co., Boston, MA, 1992.
22. R. Shannon: *Acta Crystallogr.*, 1976, vol. A32, pp. 751–67.
23. M. Hillert, B. Jansson, and B. Sundman: *Z. Metallkd.*, 1988, vol. 79, pp. 81–87.
24. I.-H. Jung: Ph.D. Thesis, École Polytechnique de Montréal, Montreal, 2003.
25. I.-H. Jung, S. Deckerov, and A. Pelton: *Metall. Mater. Trans. B.*, 2004, vol. 35B, pp. 877–89.
26. I. Abs-Wurmbach: *Contrib. Mineral. Petrol.*, 1980, vol. 71, pp. 393–99.
27. I. Abs-Wurmbach, T. Peters, K. Langer, and W. Schreyer: *Neues Jahrb. Mineral. Abh.*, 1983, vol. 146, pp. 258–79.
28. K. Schwerdtfeger and A. Muan: *Trans. Metall. Soc. AIME*, 1967, vol. 239, pp. 1114–19.
29. E. Aukrust and A. Muan: *Trans. Met. Soc. AIME*, 1964, vol. 230, pp. 1395–99.
30. K. Ono, T. Ueda, T. Ozaki, Y. Ueda, A. Yamaguchi, and J. Moriyama: *Nippon Kinzoku Gakkaishi*, 1971, vol. 35, pp. 757–63.
31. P. Franke and R. Dieckmann: *J. Phys. Chem. Solids*, 1990, vol. 51, pp. 49–57.
32. R. Subramanian and R. Dieckmann: *J. Am. Ceram. Soc.*, 1993, vol. 76, pp. 2065–75.
33. SGTE alloy database. <http://www.sgte.org>. Accessed Oct 2007.
34. A. Muan: *Am. J. Sci.*, 1959, vol. 275, pp. 297–315.
35. A. Muan: *Am. Mineral.*, 1959, vol. 44, pp. 946–60.
36. J. de Villiers and F. Herbstein: *Am. Mineral.*, 1967, vol. 52, pp. 20–30.
37. R. Robie, J. Huebner, and B. Hemingway: *Am. Mineral.*, 1995, vol. 80, pp. 560–75.
38. J.-H. Huang and E. Rosén: *Phys. Chem. Miner.*, 1994, vol. 21, pp. 228–33.
39. O. Florke: *Ber. Dtsch. Keram. Ges.*, 1961, vol. 38, pp. 89–132.
40. A. Morris and A. Muan: *J. Met.*, 1966, vol. 18, pp. 957–60.
41. C. Henderson, K. Knight, S. Redfern, and B. Wood: *Science*, 1996, vol. 271, pp. 1713–15.
42. S. Redfern, C. Henderson, B. Wood, R. Harrison, and K. Knight: *Nature*, 1996, vol. 381, pp. 407–09.
43. S. Redfern, C. Henderson, K. Knight, and B. Wood: *Eur. J. Mineral.*, 1997, vol. 9, pp. 287–300.
44. S. Redfern: *Physica B*, 1998, vols. 241–243, pp. 1189–96.
45. S. Redfern, K. Knight, C. Henderson, and B. Wood: *Mineral. Mag.*, 1998, vol. 62, pp. 607–15.
46. H. Annersten, J. Adetunji, and A. Filippidis: *Am. Mineral.*, 1984, vol. 69, pp. 1110–15.
47. O. Ballet, H. Fuess, and T. Fritzsche: *Phys. Chem. Miner.*, 1987, vol. 15, pp. 54–58.
48. K. Schwerdtfeger and A. Muan: *Trans. Met. Soc. AIME*, 1966, vol. 236, pp. 201–11.
49. T.-K. Jeong, G. Jung, K.-Y. Lee, Y.-B. Kang, H.K.D.B. Bhadeshia, and D.-W. Suh: *Mater. Sci. Technol.*, 2014, vol. 30, pp. 1805–14.
50. Y. Kim and J. Lee: *J. Mater. Sci.*, 2012, vol. 47, pp. 8477–82.
51. S. Deckerov, I.-H. Jung, Y.-B. Kang, E. Jak, V. Swamy, D. Kevorkov, and A. Pelton: F*A*C*T Consortium 2002 Progress Report. Technical Report, École Polytechnique de Montréal, Montréal, QC, 2002.
52. Y.-B. Kang, I.-H. Jung, S. Deckerov, A. Pelton, and H.-G. Lee: *ISIJ Int.*, 2004, vol. 44, pp. 965–74.
53. S. Ban-Ya, M. Hino, and N. Yuge: *Tetsu Hagane*, 1985, vol. 71, pp. 853–60.
54. H. Fujita and S. Maruhashi: *Tetsu Hagane*, 1970, vol. 56, pp. 830–51.
55. Y. Kojima and K. Sano: *Tetsu Hagane*, 1965, vol. 51, pp. 1122–30.
56. V. Schenck and G. Wiesner: *Arch. Eisenhüttenwes.*, 1956, vol. 27, pp. 1–11.
57. F. Körber and W. Oelsen: *Mitt. K. Wilh. Inst. Eisenforsch.*, 1933, vol. 15, pp. 271–391.
58. P. Riboud and A. Muan: *Trans. Metall. Soc. AIME*, 1962, vol. 224, pp. 27–33.
59. J.C. Herty Jr. and M. Royer: Technical Report, Technical Paper No. 523, U.S. Bureau of Mines, 1932.
60. R. Hay, J. White, A. McIntosh, and W. Scot: *Iron Steel Inst.*, 1934–1935, vol. 42, pp. 99–104.
61. W. Maddocks: *Iron and Steel Inst. (Lond.)*, 1935, vol. 24, pp. 51–68.
62. P. Carter, A. Murad, and R. Hay: *Philips Res. Rep.*, 1952–1953, vol. 60, pp. 123–31.
63. H. Bell: *J. Iron Steel Inst.*, 1963, vol. 201, pp. 116–21.
64. A. Muan and E. Osborn: *Phase Equilibria Among Oxides in Steelmaking*, Addison-Wesley Publishing Co., Inc., Reading, MA, 1965.
65. A. Muan and S. Somiya: *Am. Mineral.*, 1961, vol. 46, pp. 364–78.